Pencil-drawing on Nitrogen and Sulfur co-doped carbon paper: An Effective and Stable host to pre-store Li for High-performance Lithium–air Batteries

Dongdong Li [a,†], ***Shuaishuai Zhang*** [a,†], ***Qian Zhang*** [a,†], ***Payam Kaghazchi*** [b], ***Haocheng Qi*** [a, d], ***Jie Liu*** [a], ***Ziyang Guo**** [a], ***Lei Wang**** [a], ***and Yonggang Wang*** [c]

[a] *Key Laboratory of Eco-chemical Engineering, Taishan scholar advantage and characteristic discipline team of Eco chemical process and technology, College of Chemistry and Molecular Engineering, Qingdao University of Science and Technology, Qingdao 266042, P. R. China.*
[b] *Forschungszentrum Jülich GmbH, Institute of Energy and Climate Research (IEK-1), Materials Synthesis and Processing, Jülich, 52425, Germany.*
[c] *Department of Chemistry, Shanghai Key Laboratory of Molecular Catalysis and Innovative Materials, Fudan University, Shanghai 200433, P. R. China.*
[d] *State Key Laboratory of Inorganic Synthesis and Preparative Chemistry, College of Chemistry, Jilin University, Changchun 130012, P. R. China.*
†These authors contributed equally to this work (D. Li, S. Zhang and Q. Zhang).
* Corresponding author. Tel & Fax: 0086-0532-84023409
E-mail address: *zyguo@qust.edu.cn; inorchemwl@126.com*

Abstract: Metallic lithium (Li) is regarded as the ultimate anode for high-energy-density rechargeable batteries due to its highest theoretical capacity and most electronegative potential. However, there are serious challenges before practical application of Li metal batteries (*e. g.* Li–air batteries), including the dendritic Li formation and infinite variation of electrode dimension. Herein, nitrogen (N) and sulfur (S) co-doping carbon paper (NS-CP) is synthesized and further modified with a graphite-based layer (GL) by pencil-drawing. The as-prepared GL modified NS-CP (GL/NS-CP) is applied to pre-store Li through the heating-infusion method and Li-GL/NS-CP electrode is obtained. Experimental and theoretical results have demonstrated that N, S co-doping can effectively enhance the lithiophilicity of CP to ensure the uniform Li deposition. In addition, GL presents excellent Li wettability to rapidly syphon molten Li. Moreover, abundant pores in GL/NS-CP can accommodate enough Li to alleviate electrode volume change and lower local current density to restrain Li dendrites. Compared with pure Li anode, Li-GL/NS-CP electrode shows more stable voltage curves with lower overpotential (20 mV for 600 cycles). As a result, Li–air batteries with Li-GL/NS-CP anodes also exhibit the satisfying cycling life. These results have shed a new light on the development of Li anodes.

Keywords: (N and S co-doped carbon paper, Graphite-based layer, Stable Li host, Thermal infusion method, Li–air batteries)

1. Introduction

Lithium (Li) metal, which exhibits a super-high specific theoretical capacity (3860 mAh g^{-1}), light weight density (0.53 g cm^{-3}) and most electronegative potential (-3.04 V *vs* standard hydrogen electrode), is regarded as ultimate anode for high-energy-density rechargeable batteries [1-4]. Hence, Li-metal batteries (LMBs), especially for Li–air batteries, hold great promises for potential applications in portable electronic, electrical transportation, and grid storage [5-8]. However, the practical application of Li metal is still stagnant and faces many serious challenges. One of the toughest issues is the formation of dendritic Li and the infinite variation of electrode dimension during repeated Li plating/stripping process [9]. The uncontrollable Li dendrites can not only cause the rapid capacity loss of LMBs, but also give rise to the serious thermal runaway and potential explosion hazards [10-12].

Moreover, the huge electrode dimension change, which origins from the features of the uneven deposition and the “hostless” of the metallic Li, can further deteriorate the electrochemical performance of LMBs and even break the internal structure of the batteries [13-15]. Therefore, mitigating the growth of dendritic Li and the change of electrode dimension is extremely urgent since they have the potential to realize the practical application of LMBs [16].

To solve the above problems, continuous researches have been made to deepen our understanding of the reaction mechanism on the Li anode and impede the dendritic Li growth during the charge/discharge process. One common strategy for Li dendrite inhibition is to construct the stable solid electrolyte interphase (SEI) by employing the modified liquid electrolyte (*e. g.* adding functional additives, Li salts, or new solvents) or exploiting the artificial protection films [17-23]. However, these interface layers are usually not enough robust and gradually broken by the dramatical volumetric change during long-term cell operation. Subsequently, a series of the solid-state electrolytes have been designed and used in LMBs to effectively suppress the penetration of Li dendrites and enhance the battery safety [24-29]. Unfortunately, the huge interface impedance, low ion conductivity or high operating temperature is still the huge challenges for the application of the solid-state electrolytes in LMBs. Furthermore, the solid-state electrolytes also cannot solve the problem of the infinite dimension change derived from the “hostless” nature of Li at the high capacity during the Li deposition/dissolution process. Hence, pre-storing enough Li within the three dimensional (3D) porous host has been recently regarded as the promising anode candidate for LMBs [30]. A series of porous scaffolds, including the various 3D porous Cu matrixes, carbon nanofiber-based current collectors, functional 3D graphene-based conductive frameworks and carbon/metal-based composites, have been applied as the host to accommodate Li through the electrodeposition method [31-36]. However, the electrodepositing approach to store Li can induce the slight inhomogeneous deposition of metallic Li and even make the fabrication process of these anodes complicated and inefficient. Very recently, a simple heating infusion method has been developed by embedding the molten Li into the lithiophilic skeletons, which not only effectively mitigates the dendritic formation and huge volume expansion during cycling, but also avoids the very tedious fabrication process [37, 38]. Many stable hosts, such as reduced graphene oxide (rGO), ZnO-coated carbonized wood, 3D nickel (Ni) foam, Li/Si-coating porous carbon scaffold, carbon fiber/Ag, 3D Cu foam with Cu nanowires, CoO nanofiber decorated Ni foam, TiC/C core/shell nanowire arrays, ZnO/carbon fiber cloth, Co_3O_4-nitrogen doping carbon (NC)/carbon fiber cloth and nitrogen, phosphorus co-doped carbon cloth (NPCC) and so on, have been applied to construct the high-performance Li-based anodes [39-51]. It can be found that most of the 3D scaffolds for these Li hosts are carbon framework which generally shows the inferior lithiophilicity. Hence, most of these 3D carbon frameworks are usually surface-coated with ZnO or Si layer to enhance the binding ability with Li. However, these alloy-type coating phases not only have large mass density and high cost, but also potentially reduce specific capacity and stability of Li based electrodes. Therefore, developing new and effective strategies to modulate the surface stability and lithiophilicity of 3D carbon skeleton is very crucial for constructing the high-performance Li composite anode.

Herein, nitrogen (N) and sulfur (S) co-doped carbon paper (NS-CP) has been prepared through pyrolysis of polypyrrole (PPy) rooted CP coupled with thiourea, which is modified with graphite-based layer (GL) by pencil-drawing and further reacts with molten Li to fabricate Li based GL modified NS-CP (Li-GL/NS-CP) electrode. N, S co-doping can effectively enhance the surface lithiophilicity of CP and thus promote the uniform nucleation of Li on NS-CP. In addition, GL shows good wettability for molten Li to obviously improve the infusion rate of metallic Li into NS-CP framework. Moreover, the porous 3D carbon framework not only can effectively reduce the real current density to suppress the Li dendrite, but also show the superior thermal and electrochemical stability. Li-GL/NS-CP electrode in the symmetric batteries exhibits extremely stable voltage curves with very low overpotentials and dendrite-free morphology with limited volume change during Li plating/stripping processes. When Li-GL/NS-CP anodes are further coupled with air electrodes, $LiFePO_4$ or sulfur (S) cathodes, all the constructed full batteries show much better electrochemical performances (such as higher rate capability, larger capacity, lower voltage polarization or longer cycling life) than the corresponding bare Li based cells.

2. Experimental Section

NS-CP preparation

Firstly, 1.064 g lithium perchlorate and 2.12 g sodium carbonate were uniformly mixed in 100 mL H_2O. After that, 1.04 mL pyrrole and 1 g thiourea were slowly adding in the above aqueous solution under enough stirring for 30 minutes. In addition, the carbon paper (CP) was treated with concentrated acid and washed by water for several times. The obtained CP was further heated at 100 °C for 10 h to remove residual water. Then, we used the acid-treated CP as the work electrode, Pt as the counter electrode and Ag/AgCl as the reference electrode to form the three-electrode system. This three-electrode system operated at the constant voltage (0.8 V *vs.* Ag/AgCl) for 10 min and the polypyrrole (PPy) and thiourea based CP is achieved. Finally, the treated CP was further pyrolyzed at 800 °C under Ar atmosphere for 2 h and the N, S co-doping carbon paper (NS-CP) was gotten. N-CP and S-CP were prepared as the same method without adding thiourea or pyrrole, respectively.

Li-GL/NS-CP preparation

Firstly, the as-prepared NS-CP was cut into the disk with the diameter of 12 mm. After that, the commercial 12B pencil was uniformly drawn on the NS-CP disk to form the graphite-based layer (GL) modified NS-CP (GL/NS-CP) and the detailed preparation of GL/NS-CP is given in the experimental section of supporting information. The thermal infusion process was conducted in an Ar-filled glove box (< 0.1 ppm O_2 and < 0.1 ppm H_2O). Specifically, the Li film was carefully polished until it showed the very shiny surface. Then, the polished Li film was subsequently transferred into the stainless-steel container and further heated on the hotplate at 270 °C. Finally, the GL/NS-CP was directly contacted with the molten Li and rapidly absorbed the molten Li in the whole skeleton to form the Li-GL/NS-CP electrode.

Assembly of the batteries and electrochemical measurements

We firstly fabricated symmetric batteries to clarify Li stripping/plating performance. Specifically, Li-GL/NS-CP|1.0 M bis (trifluoromethane) sulfonamide lithium salt (LiTFSI) in 1:1 v/v dimethoxyethane (DME) and 1, 3-dioxolane (DOL) with 2.0 wt% lithium nitrate ($LiNO_3$) additive|Li-GL/NS-CP were sealed into the CR2016-type coin configuration in the Ar-filled glove box. The bare Li based symmetric cells were also assembled at the same condition. The fabrications of the full cells (*e. g.* Li–LFP and Li–air batteries) are as follow: firstly, the LFP, and KB/Ru cathodes were designed and the corresponding preparations were given in the Supporting Information. For the assembly of the Li–LFP full cells, the LFP cathode and Li-GL/NS-CP or pure Li anode were separated by the separators filled with electrolytes and then sealed into the CR2016 coin-type configurations. The Li–LFP system used the 1 M lithium hexafluorophosphate ($LiPF_6$) in 1:1 v/v EC/DEC as electrolyte. In addition, Li–air batteries were assembled by using the Li-GL/NS-CP or pure Li metal as anode, Ketjenblack (KB)/ruthenium (Ru) composite as cathode and 1.0 M LiTFSI/TEGDME as electrolyte. All the cells were cycled in the eight-channel LAND battery test system (Wuhan Land Electronic Co. Ltd). Moreover, all the cathode preparation, the additional electrochemical measurements, and characterization instrumentation were given in supporting information.

3. Results and Discussion

Carbon paper (CP) has been considered as a promising framework to store Li because of its porous structure and superior surface conductivity. Nevertheless, the lithiophobic property of CP makes it hardly syphon molten Li (**Fig. S1**). To enhance the lithiophilicity of CP, nitrogen (N) and sulfur (S) co-doped CP (NS-CP) are synthesized through electrodeposition and subsequent carbonation processes of polypyrrole (PPy) rooted CP with the existence of thiourea (**Fig. 1a**). The resulting NS-CP matrix can react with molten Li, but the corresponding reaction rate is not fast (the infusion of molten Li into the whole NS-CP is about 22 s, **Fig. S2**). Recent report has demonstrated that drawing the graphite-based layer (GL) on solid electrolytes by pencil can effectively enhance their surface wettability for molten Li [38]. Hence, as illustrated in **Fig. 1a**, we have further used a 12B pencil to paint a GL on the surface of NS-CP to form GL modified NS-CP (GL/NS-CP). Due to the synergy of GL and NS-CP, molten Li has been rapidly infused into the whole scaffold of GL/NS-CP within 6s to obtain Li based GL/NS-CP (Li-GL/NS-CP) electrode (**Fig. S3**). Detailed morphology information of Li-GL/NS-CP and its precursors is detected by scanning electron microscope (SEM) and transmission electron microscope (TEM) measurements. There are many carbon fibers in the original CP (**Fig. 1b**) and the surfaces of these carbon fibers are very smooth (Insert of **Fig. 1b**). After electrodeposition, the PPy coating layers are uniformly enwound around carbon fibers of CP (**Fig. S4**). After the following pyrolysis, the core-shell structure still exists in the NS-CP (**Fig. 1c** and **d**), indicating that calcination procedure does not destroy the pristine structure of PPy coated CP. Energy-dispersive X-ray (EDX) mapping measurement of NS-CP suggests that N, S and C elements are uniformly distributed on the carbon fiber skeleton, respectively (**Fig. 1e)**. The EDX mapping images of N-CP or S-CP are also investigated (**Fig. S5**).

To analyze the surface elements composition of NS-CP, X-ray photoelectron spectroscopy (XPS) technology is also conducted. It can be found from full XPS spectrum of NS-CP that the surface contents of N and S species are 6.09 and 1.10 %, respectively, further demonstrating the successful introduction of N and S species into the NS-CP (**Fig. S6**). **Fig. 1f** shows that the high-resolution N 1s peak can be deconvoluted into four assumed species: pyridinic N (398.3 eV), pyrrolic N (400.3 eV), graphited N (400.9 eV), and oxidized pyridinic N (403.1 eV). In addition, the high-resolution S 2p peak presents three fitting bands: S $2p_{3/2}$ peak at 163.6 eV, S $2p_{1/2}$ peak at 164.9 eV and S-O peak at 168.5 eV (**Fig. 1g**). When typical thin-film GL with the interplanar spacing of 0.34 nm has been further drawn on NS-CP (**Fig. 1h**), the surface of GL/NS-CP becomes flatter and blacker compared with the pristine CP (**Fig. 1i** and **S7**). The average thickness of the GL onto the surface of GL/NS-CP is ~5 μm (**Fig. S8**). After the process of molten Li infusion, Li-GL/NS-CP exhibits a golden and smooth surface (**Fig. 1j**). The cross-sectional SEM image shown in **Fig. S9** indicates that the molten Li can be uniformly penetrated into the whole scaffold and the thickness of Li-GL/NS-CP is about 187 μm. Additionally, the X-ray diffraction (XRD) result of Li-GL/NS-CP (**Fig. S10**) further indicates that metallic Li and LiC_x phases are formed on GL/NS-CP after reacting with molten Li. It can be observed from **Fig. S11** that the oxygen surface content of GL/NS-CP is obviously higher than that of NS-CP, suggesting that GL coating can effectively enhance the surface content of oxygenic groups on NS-CP. More interestingly, the N/S mass ratio in the bulk of GL/NS-CP is ~0.81, which is lower than that (~2.23) on the surface of GL/NS-CP (**Tab. S1**). This result indicates that the distributions of N and S elements in the bulk and on the surface of GL/NS-CP are different.

The electrochemical Li plating/stripping performance of Li-NS-CP electrode was firstly studied in the symmetric configuration with 1.0 M LiTFSI in 1:1 *v/v* DOL/DME with 2.0 wt% $LiNO_3$ electrolyte. Li-N-CP, Li-S-CP and bare Li anodes were also tested under the same condition for comparison. **Fig. 2a** gives the electrochemical performances of Li-NS-CP, Li-N-CP, Li-S-CP and bare Li anodes in symmetric batteries at different current densities with a fixed Li stripping/plating capacity of 1.0 mAh cm^{-2} (**Fig. 2a**). As shown in **Fig. 2a**, the overpotentials of Li-N-CP electrode at 0.5, 1.0, 3.0 and 5.0 mA cm^{-2} are ~40, 95, 135 and 220 mV, respectively, which are similar to these of Li-S-CP anode. However, all the voltage polarizations of bare Li electrode are always higher than these of Li-N-CP or Li-S-CP anode at the current densities varying from 0.5 to 5.0 mA cm^{-2}. Especially at 5.0 mA cm^{-2}, the voltage curves of the Li anode exhibit the huge overpotential (**Fig. 2a**), which may be caused by the uneven deposition of metallic Li. These phenomena indicate that N-CP and S-CP exhibit better lithiophilicity compared with Li anode. Moreover, the overpotentials of the Li-NS-CP electrode are smallest among four Li-based anodes at all the current densities, which are only within 25, 40, 90 and 136 mV at 0.5, 1.0, 3.0 and 5.0 mA cm^{-2}, respectively. The outstanding rate performance of the Li-NS-CP electrode may be mainly attributed to the positive synergy effect of the N, S co-doping for Li stripping/plating process. The cycling performance of the Li-NS-CP, Li-N-CP, Li-S-CP and pure Li electrodes is also recorded through the galvanostatic voltage curves at 3.0 mA cm^{-2} with the fixed capacity of 1.0 mAh cm^{-2} (**Fig. 2b** and **S12**). It can be found from **Fig. 2b** that the Li stripping/plating platforms of both Li-NS-CP, Li-N-CP and Li-S-CP electrodes are almost constant over 100 cycles, while bare Li electrode exhibits the irregular and dramatic oscillation voltage profiles after only 80 cycles with the largest voltage polarization (~340 mV) among these anodes, which also highlights that the N or S-doping matrix can effectively enhance the lithiophilic features. More interestingly, it should be noted that the average overpotential of Li-NS-CP electrode is only around 90 mV during 100 cycles (**Fig. 2b** and **S12**), which is lower than these of Li-S-CP anode (~135 mV) and Li-N-CP anode (~158 mV). These results demonstrate that N, S co-doping greatly improves the surface lithiophilicity and thus effectively facilitates the reversibility during the repeated Li stripping/plating process. To further clarify the relationship between heteroatom dopant and surface lithiophilicity of the corresponding carbon matrixes, the binding energy (BE) of Li at various possible sites on pure, N-doped, S-doped and N, S co-doped graphene are investigated by density functional theory (DFT) calculations (**Fig. S13** and **Tab. S2**). **Fig. 2c-f** give the most favorable Li adsorption sites for pristine and doped graphene and their corresponding charge density difference plots. It is found that Li binds only to C atoms in the pristine graphene (**Fig. 2c**) and the strongest BE of Li at various possible sites on pure graphene is only -0.27 eV (**Tab. S2**), indicating a weak interaction between a Li atom and bare graphene. For the N-doped graphene, the Li atom binds to both N and C atoms which was saturated by H at the edge (**Fig. 2d**) and the BE in this case is calculated to be 0.69 eV stronger than that in the pristine case (**Tab. S2**). In the case of S-doped graphene, the BE at the most favorable Li adsorption site where Li atom can interact with two saturated C and S atoms is -1.46 eV (**Fig. 2e** and **Tab. S2**), which is also much stronger compared with the pristine case. In addition, it should be noted that the charge density difference in the regions between Li and N-doped graphene is similar to that between Li and S-doped graphene (**Fig. 2d** and **e**). However, there is a small negative charge on S in the latter case showing an indirect electron transfer (via C atoms) from Li to S. More interestingly, the interaction of Li with N and S atom in N, S co-doped graphene is obviously higher than that in N- or S-doped graphene and the BE for Li over this N, S co-doped case is strongest (-1.72 eV) among four graphene-based cases (**Fig. 2f** and **Tab. S2**), which indicates that synergic effect of N and S co-doping apparently improve the interaction of Li with our graphene-based matrix. This is because there is a larger negative charge on the S atom in the N, S co-doped case than that in the S-doped case. Moreover, a larger electrostatic attraction between S and Li atoms is expected in the former case. It is well known that the binding energy between Li and graphene-based matrix is directly related to surface lithiophilicity of these carbon frameworks [51]. Hence, these results further demonstrate that the co-existence of N and S can effectively enhance lithiophilicity of carbon paper, which is in accordance with the above molten Li infusion rate and electrochemical performance results.

Due to the abundant surface oxygenic groups, GL coating have made GL/NS-CP present excellent Li wettability to rapidly syphon molten Li. Moreover, recent reports also have confirmed that the oxygen-containing groups usually show the strong binding energy to Li and thus improve the surface lithiophilicity [38, 40, 48]. To further explore the favorable contribution of GL coating for the Li stripping/plating process, the electrochemical performances of Li-GL/NS-CP, Li-NS-CP, Li based GL coating CP (Li-GL/CP) and bare Li electrodes are also investigated in the symmetric batteries. **Fig. 3a** and **b** give the voltage profiles of Li-GL/NS-CP, Li-NS-CP and bare Li anodes at different current densities with the same Li stripping/plating capacity of 1.0 mAh cm^{-2}. As shown in **Fig. 3a**, bare Li electrode displays large overpotential (~52 mV) and has an obviously increasing overpotential of more than 170 mV after 228 cycles. Compared with the bare Li anode, the Li-GL/CP anode shows the lower voltage polarization (~45 mV) and longer cycling life (over 250 cycles), which indicates that GL coating promotes the reversible Li stripping/plating during cycles (**Fig. S14**). In addition, the discharge/charge profiles of Li-NS-CP electrode are also almost uncharged over 590 cycles, and its average overpotential (~25 mV) is obviously lower than Li-GL/CP and Li anodes over the whole cycling (**Fig. 3a** and **S15**), which further indicates that N, S co-doping can obviously enhance the surface lithiophilicity. Moreover, Li-GL/NS-CP anode also exhibits an extremely stable and small overpotential of ~20 mV over 600 cycles (**Fig. 3a** and **S15**), which is much better than all the above anodes and most of the recently reported Li-based anodes (**Tab. S3**). The superior electrochemical performance of Li-GL/NS-CP can be ascribed to the synergistic effect of N, S co-doping and GL coating. Even when the applied current density reaches 1.0 mA cm^{-2}, both Li-GL/NS-CP and Li-NS-CP anodes based symmetrical batteries keep very flat voltage profiles during cycles, and the corresponding average voltage hysteresis of Li-GL/NS-CP and Li-NS-CP electrodes throughout the whole cycles are ~30 and 40 mV, respectively (**Fig. 3b** and **S16**). In contrast, the overpotential of the symmetrical cell with bare Li metal anode increases to 220 mV at the 300th cycle (**Fig. 3b**), which can be attributed to the rapidly growth of Li dendrites and even the internal short circuit over cycling. To evaluate the Coulombic efficiency of these NS based hosts, the GL/NS-CP, NS-CP or Cu foil is used as the working electrode and Li metal as the counter electrode with 1.0 M LiTFSI in 1:1 v/v DME and DOL with 2.0 wt% $LiNO_3$ electrolyte to form the half batteries. These cells are first cycled at 0-1.0 V (*vs* Li^+/Li) at 0.05 mA for 3 cycles for activation and SEI formation. The following procedures are to deposit the fixed amount of Li (1.0 mAh cm^{-2}) at 1.0 mA cm^{-2} and strip Li until the voltage reaches up to 1.0 V (*vs* Li^+/Li) at the same current. Although both GL/NS-CP and NS-CP electrodes deliver the superior average Coulombic efficiency of ~99.5 % and 98.5 % over 100 cycles, the Coulombic efficiency of NS-CP electrode during the whole cycling shows more irregular oscillations than GL/NS-CP electrode. On the contrast, Cu electrode exhibits a dramatically fluctuated Coulombic efficiency below 80 % after 52 cycles (**Fig. 3c**). The best Coulombic efficiency of GL/NS-CP electrode among three matrixes is mainly due to the enough lithiophilic sites, good conductivity and porous/stable structure in GL/NS-CP. To further clarify the interfacial reaction mechanism, the electrochemical impedance spectroscopy (EIS) of Li-GL/NS-CP, Li-NS-CP and pure Li anodes based symmetric batteries before and after 10 cycles are also studied at 1.0 mA cm^{-2} with a limited capacity of 1.0 mAh cm^{-2} (**Fig. 3d** and **S17**). It is well known that the semi-circle in high frequency region of EIS profile is corresponding to the charge-transfer resistance on the anode surface and interfacial resistance of SEI film [52]. For the symmetrical cell with bare Li anode, the interfacial resistance is as high as 374.9 Ω before cycling and rapidly decreases to 69.1 Ω after 10 cycles (**Fig. 3d** and **S17**). The obvious decrease resistance of Li anode is associated with its enhanced surface area which is derived from the decomposition of SEI layer and the Li dendrites growth during cycles. On the contrast, the interfacial resistances of Li-GL/NS-CP and Li-NS-CP electrodes are 33.4 and 87.6 Ω at the initial stage, and slightly drop to 16.5 and 25 Ω after 10 cycles, respectively. These results indicate that Li-GL/NS-CP and Li-NS-CP anodes have more stable SEI film and faster electrochemical Li stripping/plating kinetics than pure Li anode over cycles. Moreover, the different interfacial resistances of Li-GL/NS-CP and Li-NS-CP anodes before cycling may be related to their different interfacial states (**Fig. 1j** and **S18**). More interestingly, when fully charged to 1.0 V, the Li-GL/NS-CP anode even displays the super-high specific capacity 3485 mAh g^{-1} based on the mass of molten Li infused at the current density of 0.5 mA cm^{-2} (**Fig. S19**), which is higher than most of the Li-based anodes in recent reports (**Tab. S4**). This phenomenon can be ascribed to enough porosities and low mass density of carbon framework in Li-GL/NS-CP electrode.

To study the morphology variation of Li-GL/NS-CP and bare Li electrodes during the Li stripping/plating process, their SEM images after different Li stripping/plating amounts are firstly tested at a current density of 1.0 mA cm^{-2} in the symmetric batteries. As shown in **Fig. 4a**, the surface of Li-GL/NS-CP becomes rough and the basic framework of GL/NS-CP also re-emerges with the residual Li particles around the carbon fibers at Li stripping capacity of 5.0 mAh cm^{-2}, indicating the stable skeleton of Li-GL/NS-CP anode during Li striping process. When 3.0 mAh cm^{-2} Li is deposited back, the voids between these fibers are filled with metallic Li and the surface of Li-GL/NS-CP electrode is uniformly coated with a mass of Li bulks (**Fig. 4a**), suggesting that GL/NS-CP matrix can induce the homogeneous nucleation of metallic Li during Li plating process. When the additional capacity of 2.0 mAh cm^{-2} Li continues to be plated back, the surface of the ultimate Li-GL/NS-CP becomes very smooth without any dendritic Li (**Fig. 4a**), which is in agreement with the original Li-GL/NS-CP (**Fig. 1j**). These results demonstrate that Li-GL/NS-CP anode has the superior reversibility over Li stripping/plating process. In addition, the cross-section SEM images of Li-GL/NS-CP over different Li stripping/plating stages are also observed. No matter after 5 mAh cm^{-2} Li dissolution or 5 mAh cm^{-2} Li deposition, the thickness of the Li-GL/NS-CP anode can keep around 190 μm (**Fig. 4b**), which is almost the same as that of the pristine Li-GL/NS-CP electrode (**Fig. S7**). For comparison, the pure Li anode is also tested under the same condition (**Fig. 4c** and **d**). It can be found from **Fig. 4c** that the surface of metallic Li electrode becomes very rough and even is covered with several obvious Li dendrites after stripping away and replating back 5 mAh cm^{-2} Li, which indicates the inferior cycle stability of Li anode. Moreover, the bare Li anode exhibits the huge volume changes over the whole Li stripping/plating process (**Fig. 4d**). To further clarify the fact that the huge electrode dimension change usually results in the internal short circuit of batteries, the Li-based anode|separator|Cu mesh|separator|Li-based cathode symmetrical battery has been assembled. The open circuit voltage (OCV) between Li-based electrode and Cu electrode (OCV$_{Cu/Li}$) is recorded when this symmetrical cell is continuously charged at the current density of 5.0 mA cm^{-2} (**Fig. 4e** and **f**). It can be observed from **Fig. 4e** that the charge voltage profile of the Li-GL/NS-CP based cell is very stable and the corresponding OCV$_{Cu/Li}$ can keep almost unchanged over 48000 s. On the contrast, the OCV$_{Cu/Li}$ of the bare Li based battery shows the obvious drop and the corresponding charge voltage curve occurs the drastic fluctuation after only 9000 s (**Fig. 4f**), which indicates that the separator is punctured by the dendritic Li and huge thinckness change of Li anode. These above results suggest that the synergy of the porous/conductive structure and enough lithiophilic sites in Li-GL/NS-CP can not only effectively guide the uniform Li deposition, but also suppress the dimension volume change over cycling.

To further clarify the morphology evolution of the Li-GL/NS-CP and Li anodes over cycles, the surface SEM characterization is also carried out after 10 cycles with a limited capacity of 1.0 mAh cm^{-2} at different current densities. As shown in **Fig. 5a**, the top SEM image of the Li-GL/NS-CP electrode exhibits the flat and smooth surface without obvious dendrites after 10 cycles at the current density of 0.5 mA cm^{-2}. Even at the higher current densities of 1.0 and 3.0 mA cm^{-2}, the surface of the Li-GL/NS-CP anode is still relatively clear over 10 cycles (**Fig. 5b** and **c**). On the contrast, the bare Li anode shows the rough surface morphology after 10 cycles at the low applied current of 0.5 mA cm^{-2} (**Fig. 5d**). In addition, the surface roughness of Li electrode becomes more serious when the current density increases to 1.0 mA cm^{-2} (**Fig. 5e**). Moreover, there are many Li dendrites stacked on the whole Li electrode surface at 3 mA cm^{-2} over 10 cycles (**Fig. 5f**). On the other hand, *in-situ* optical microscopy technology has also been applied to further study the cross-section morphological changes of Li-GL/NS-CP and Li electrodes at the fixed capacity of 1 mAh cm^{-2} with the current of 3 mA cm^{-2} during different cycles (**Fig. 5g** and **h**). As shown in **Fig. 5g**, the surface of Li-GL/NS-CP electrode is very smooth without any obvious Li dendrites and its corresponding thickness change is very limited in the whole 10 Li stripping/plating cycles. On the contrast, the bare Li anode exhibits more and more rough surface with the continuously generated Li dendrites as the number of cycles increases and the electrode dimension shows the huge deformation throughout the total cycles (**Fig. 5h**). The above results further reveal the highly reversible Li stripping/plating behavior of the Li-GL/NS-CP anode over cycling.

Because of the superior Li stripping/plating performance of the Li-GL/NS-CP anode, $LiFePO_4$ (LFP) electrodes have been coupled with Li-GL/NS-CP anodes to assemble the full batteries. **Fig. 6a** shows that the discharge capacity of the Li-GL/NS-CP|LFP battery is as high as 127 mAh g^{-1} on the initial cycle and can still maintain 125 mAh g^{-1} at 2.0 C (1 C = 170 mA g^{-1}) after 200 cycles (the first cycles of both cells in **Fig. 6a** are are the activation process at the low current of 0.5 C). However, for the Li|LFP battery, the special capacity is 114 mAh g^{-1} at the initial cycle and rapidly decreases to 45 mAh g^{-1} after cycling under the same condition (**Fig. 6a**). **Fig. 6b** further indicates that rate performance of the LFP based battery with Li-GL/NS-CP anode is much better compared with the cell with bare Li anode. In addition, it can be also observed from the voltage curves shown in **Fig. 6c** that the Li-GL/NS-CP|LFP battery shows higher capacity and lower overpotential than the Li|LFP battery over the charge/discharge process at 0.5 C. *In situ* FT-IR technology has also been applied to clarify the reversibility of Li-GL/NS-CP|LFP battery over cycling (the detailed experimental procedure is given in the Supporting Information). As shown in **Fig. 6d**, the bands at 1150 ($\nu_{C\text{-}O}$) and 1799 ($\nu_{C=O}$) cm^{-1} from free EC molecules and these peaks around 1253 ($\nu_{C\text{-}O}$) and 1737 ($\nu_{C=O}$) cm^{-1} from free DEC molecules are gradually weakening, while the bands from Li^+-solvating EC and DEC molecules ($\nu_{C\text{-}OLi^+}$ at 1082 cm^{-1} and $\nu_{C=OLi^+}$ at 1715 and 1764 cm^{-1}) are obviously strengthening during charge process [53, 54]. Over discharge, these free solvent molecules reversibly increase and the Li^+-solvating molecules have the opposite changes. Meanwhile, the absorbance of P-F bands at 833 cm^{-1} and PO_4^{3-} at 652 cm^{-1} also shows the reversible changes over cycles in Li-GL/NS-CP|LFP battery [54]. These results further confirm that the Li-GL/NS-CP|LFP batteries have good cyclic reversibility.

On the other hand, such an excellent Li-GL/NS-CP electrode is also applied in Li–air batteries under ambient air (RH < 15 %) to assess its practical application [55].

For comparison, the pure Li anode is also tested at the same condition. Moreover, Li-GL/NS-CP anode has also been paired with the KB/Ru based air cathodes (the preparation and characterization of KB/Ru cathodes are given in the supporting information and **Fig. S20**) to construct the Li–air batteries. **Fig. 7a-d** give the cycling stability of the Li–air batteries with the Li-GL/NS-CP and bare Li anodes at a current density of 500 mA g^{-1} with a fixed capacity of 1000 mAh g^{-1}. As shown in **Fig. 7a**, the Li–air battery with Li-GL/NS-CP anode exhibits the stable and reproducible discharging/charging voltage profiles over 100 cycles. The slight charge voltage decrease after 90 cycles of Li-GL/NS-CP based Li–air battery may be attributed to air-attacking on Li anode or the assistance of increased humidity in ambient air (**Fig. S21**). In addition, it can be observed from **Fig. 7b** that the overpotentials for Li–air battery with Li-GL/NS-CP anode are < 1.3 V over 100 cycles. However, the bare Li anode-based Li–air battery can only be normally cycled for 40 cycles (**Fig. 7c**) and its discharge terminal voltages of the bare Li anode-based Li–air batteries rapidly drop to 2.0 V after only 44 cycles (**Fig. 7d**). In addition, *ex situ* FT-IR spectra and XRD patterns have been applied to investigate the products of Li-GL/NS-CP based Li–air batteries over cycles. It can be found from **Fig. 7e** and **f** that Li_2O_2, LiOH, $LiOH•H_2O$ and Li_2CO_3 are formed during the discharge process and then almost completely decomposed over recharge in the Li–air batteries using Li-GL/NS-CP electrode. Moreover, *in situ* DEMS measurement has also been conducted to detect the gas evolution of Li–air battery with Li-GL/NS-CP anode during charge. Before *in situ* DEMS, this cell has been discharged in ambient air. It can be observed from **Fig. 7g** and **h** that a lot of oxygen and very little of carbon dioxide are also formed over recharge. **Fig. S22** also exhibits that the morphology of Li-GL/NS-CP anode is relatively stable during cycles in Li–air battery. These phenomena suggest the perfect reversibility of Li-GL/NS-CP based Li–air batteries. When Li-GL/NS-CP anodes are further paired with sulfur (S) cathodes, this constructed full cell shows much better electrochemical performances compared with the corresponding Li–S cells (**Fig. S23**). The superior electrochemical performance of these full batteries with Li-GL/NS-CP anode should be attributed to the uniform Li plating/stripping behavior without large Li dendrites of the Li-GL/NS-CP electrode over cycling.

4. Conclusion

In summary, we firstly carbonized polypyrrole rooted carbon paper (CP) in the presence of thiourea to obtain the N, S co-doped carbon paper (NS-CP), and then drew a graphite-based layer (GL) on the surface of NS-CP (GL/NS-CP) by pencil. The resulting GL/NS-CP further reacts with molten Li by a thermal infusion strategy to form Li based GL/NS-CP (Li-GL/NS-CP) electrode. The N, S co-doped porous carbon-based skeleton not only shows the extremely superior stability towards both molten Li infusion and electrochemical processes, but also promotes the nucleation of Li. Moreover, GL effectively enhances the surface wettability to Li and produces strong driving force to quickly lift molten Li into GL/NS-CP. Compared with the bare Li anode, the Li-GL/NS-CP electrode shows the longer cycling life, better rate performance, lower overpotential and smaller volume change in the symmetric batteries. When further assembled with LFP or S electrode, the Li-GL/NS-CP anode based full cells can be stably operated over cycles and display excellent rate capability. Moreover, the Li–air battery with Li-GL/NS-CP anode shows the longer cycling life (100 cycles) and smaller voltage polarization (< 1.3 V) than the bare Li electrode-based Li–air cell in ambient air. Our research provides the reasonable and low-cost strategies to obtain the high-performance Li-based anode, which is of great importance for the design of future rechargeable batteries.

Acknowledgements

The authors acknowledge funding support from the National Natural Science Foundation of China (21905151 and 51772162), the Natural Science Foundation of Shandong Province (ZR2018BB034), China Postdoctoral Science Foundation (2019M652499), Taishan scholar advantage and characteristic discipline team of Eco chemical process and technology, the State Key Laboratory of Inorganic Synthesis and Preparative Chemistry of Jilin University (2019-23) and Shanghai Science and Technology Committee (2017MCIMKF01).

References

[1] C. Y. Zhang, A. X. Wang, J. H. Zhang, X. Z. Guan, W. J. Tang, J. Y. Luo, Adv. Energy Mater. 8 (2018) 1802833.

[2] X. F. Yang, X. Li, K. Adair, H. M. Zhang, X. L. Sun, Electrochem. Energy Rev. 1 (2018) 239-293.

[3] H. Wang, D. D. Yu, C. W. Kuang, L. W. Cheng, W. Li, X. L. Feng, Z. Zhang, X. B. Zhang, Y. Zhang, Chem. 5 (2019) 313-338.

[4] J. Lu, Z. W. Chen, F. Pan, Y. Cui, K. Amine, Electrochem. Energy Rev. 1 (2018) 35-53.

[5] X. Y. Yang, J. J. Xu, Z. W. Chang, D. Bao, Y. B. Yin, T. Liu, J. M. Yan, D. P. Liu,

Y. Zhang, X. B. Zhang, Adv. Energy Mater. 8 (2018) 1702242.

[6] D. C. Lin, Y. Y. Liu, Y. Cui, Nat. Nanotech. 12 (2017) 194-206.

[7] S. W. Cranford, S. Chin, J. Q. Sun, Matter 1 (2019) 1-3.

[8] B. Dunn, H. Kamath, J.-M. Tarascon, Science 334 (2011) 928-935.

[9] Y. P. Guo, H. Q. Li, T. Y. Zhai, Adv. Mater. 29 (2017) 1700007.

[10] J. L. Ma, F. L. Meng, Y. Yu, D. P. Liu, J. M. Yan, Y. Zhang, X. B. Zhang, Q. Jiang, Nat. Chem. 11 (2019) 64-70.

[11]W. Xu, J. L. Wang, F. Ding, X. L. Chen, E. Nasybulin, Y. H. Zhang, J. -G. Zhang, Energy Environ. Sci. 7 (2014) 513-537.

[12] S. Xin, Z. W. Chang, X. B. Zhang, Y. -G. Guo, Natl. Sci. Rev. 4 (2017) 54-70.

[13] L. Fan, H. L. Zhuang, L. N. Gao, Y. Y. Lu, L. A. Archer, J. Mater. Chem. A 5 (2017) 3483-3492.

[14] K. J. Harry, D. T. Hallinan, D. Y. Parkinson, A. A. MacDowell, N. P. Balsara, Nat. Mater. 13 (2014) 69-73.

[15] B. Liu, J. -G. Zhang, W. Xu, Joule 2 (2018) 833-845.

[16] X. -B. Cheng, R. Zhang, C. -Z. Zhao, Q. Zhang, Chem. Rev. 117 (2017) 10403-10473.

[17] W. Y. Li, H. B. Yao, K. Yan, G. Y. Zheng, Z. Liang, Y. -M. Chiang, Y. Cui, Nat. Commun. 6 (2015) 7436.

[18] Y. Ouyang, Y. P. Guo, D. Li, Y. Q. Wei, T. Y. Zhai, H. Q. Li, ACS Appl. Mater. Interfaces 11 (2019) 11360-11368.

[19] K. M. Liao, S. C. Wu, X. W. Mu, Q. Lu, M. Han, P. He, Z. P. Shao, H. S. Zhou, Adv. Mater. 30 (2018) 1705711.

[20] J. F. Qian, W. A. Henderson, W. Xu, P. Bhattacharya, M. Engelhard, O. Borodin, J. -G. Zhang, Nat. Commun. 6 (2015) 6362.

[21] K. R. Adair, C. T. Zhao, M. N. Banis, Y. Zhao, R. Y. Li, M. Cai, X. L. Sun, Angew. Chem. Int. Ed. 58 (2019) 15797-15802.

[22] Z. L. Hu, S. Zhang, S. M. Dong, W. J. Li, H. Li, G. L. Cui, L. Q. Chen, Chem. Mater. 29 (2017) 4682-4689.

[23] Y. Zhao, M. Amirmaleki, Q. Sun, C. T. Zhao, A. Codirenzi, L. V. Goncharova, C. H. Wang, K. Adair, X. Li, X. F. Yang, F. P. Zhao, R. Y. Li, T. Filleter, M. Cai, X. L. Sun, Matter (2019) *https://doi.org/10.1016/j.matt.2019.06.020*.

[24] C. W. Sun, J. Liu, Y. D. Gong, D. P. Wilkinson, J. J. Zhang, Nano Energy 33 (2017) 363-386.

[25] X. F. Yang, Q. Sun, C. T. Zhao, X. J. Gao, K. Adair, Y. Zhao, J. Luo, X. T. Lin, J. N. Liang, H. Huang, L. Zhang, S. G. Lu, R. Y. Li, X. L. Sun, Energy Storage Mater. 22 (2019) 194-199.

[26] N. -W. Li, Y. -X. Yin, C. -P. Yang, Y. -G. Guo, Adv. Mater. 28 (2016) 1853-1858.

[27] J. Wang, Y. B. Yin, T. Liu, X. Y. Yang, Z. W. Chang, X. B. Zhang, Nano Res. 11 (2018) 3434-3441.

[28] L. Fan, S. Y. Wei, S. Y. Li, Q. Li, Y. Y. Lu, Adv. Energy Mater. 8 (2018) 1702657.

[29] X. G. Han, Y. H. Gong, K. Fu, X. F. He, G. T. Hitz, J. Q. Dai, A. Pearse, B. Y. Liu, H. Wang, G. Rubloff, Y. F. Mo, V. Thangadurai, E. D. Wachsman, L. B. Hu, Nat. Mater. 16 (2017) 572-579.

[30] B. Z. Yu, T. Tao, S. Mateti, S. G. Lu, Y. Chen, Adv. Funct. Mater. 28 (2018) 1803023.

[31] T. -T. Zuo, X. -W. Wu, C. -P. Yang, Y. -X. Yin, H. Ye, N. -W. Li, Y. -G. Guo, Adv. Mater. 29 (2017) 1700389.

[32] L. -L. Lu, J. Ge, J. -N. Yang, S. -M. Chen, H. -B. Yao, F. Zhou, S. -H. Yu, Nano Lett. 16 (2016) 4431-4437.

[33] Z. Y. Guo, F. M. Wang, Z. J. Li, Y. Yang, A. G. Tamirat, H. C. Qi, J. S. Han, W. Li, L. Wang, S. H. Feng, J. Mater. Chem. A 6 (2018) 22096-22105.

[34] K. Yan, Z. D. Lu, H. -W. Lee, F. Xiong, P. -C. Hsu, Y. Z. Li, J. Zhao, S. Chu, Y. Cui, Nat. Energy 1 (2016) 16010.

[35] C. -P. Yang, Y. -X. Yin, S. -F. Zhang, N. -W. Li, Y. -G. Guo, Nat. Commun. 6 (2015) 8058.

[36] R. Zhang, X. -R. Chen, X. Chen, X. -B. Cheng, X. -Q. Zhang, C. Yan, Q. Zhang, Angew. Chem. Int. Ed. 56 (2017) 7764-7768.

[37] D. C. Lin, J. Zhao, J. Sun, H. B. Yao, Y. Y. Liu, K. Yan, Y. Cui, Proc. Natl. Acad. Sci. 114 (2017) 4613-4618.

[38] Y. J. Shao, H. C. Wang, Z. L. Gong, D. W. Wang, B. Z. Zheng, J. P. Zhu, Y. X. Lu, Y. -S. Hu, X. X. Guo, H. Li, X. J. Huang, Y. Yang, C. -W. Nan, L. Q. Chen, ACS Energy Lett. 3 (2018) 1212-1218.

[39] Y. Zhang, W. Luo, C. W. Wang, Y. J. Li, C. J. Chen, J. W. Song, J. Q. Dai, E. M. Hitz, S. M. Xu, C. P. Yang, Y. B. Wang, L. B. Hu, Proc. Natl. Acad. Sci. 114 (2017) 3584-3589.

[40] D. C. Lin, Y. Y. Liu, Z. Liang, H. -W. Lee, J. Sun, H. T. Wang, K. Yan, J. Xie, Y. Cui, Nat. Nanotech. 11 (2016) 626-632.

[41] S. -S. Chi, Y. C. Liu, W, -L, Song, L. Z. Fan, Q. Zhang, Adv. Funct. Mater. 27 (2017) 1700348.

[42] R. Zhang, X. Chen, X. Shen, X. -Q. Zhang, X. -R. Chen, X. -B. Cheng, C. Yan, C. -Z. Zhao, Q. Zhang, Joule 2 (2018) 764-777.

[43] X. -Y. Yue, W. -W. Wang, Q. -C. Wang, J. -K. Meng, Z. -Q. Zhang, X. -J. Wu, X. -Q. Yang, Y. -N. Zhou, Energy Storage Mater. 14 (2018) 335-344.

[44] S. F. Liu, X. H. Xia, Z. J. Yao, J. B. Wu, L. Y. Zhang, S. J. Deng, C. G. Zhou, S. H. Shen, X. L. Wang, J. P. Tu, Small Methods 2 (2018) 1800035.

[45] Z. Liang, D. C. Lin, J. Zhao, Z. D. Lu, Y. Y. Liu, C. Liu, Y. Y. Lu, H. T. Wang, K. Yan, X. Y. Tao, Y. Cui, Proc. Natl. Acad. Sci. 113 (2016) 2862-2867.

[46] K. R. Adair, M. Iqbal, C. H. Wang, Y. Zhao, M. N. Banis, R. Y. Li, L. Zhang, R. Yang, S. G. Lu, X. L. Sun, Nano Energy 54 (2018) 375-382.

[47] C. W. Wang, Y. H. Gong, B. Y. Liu, K. Fu, Y. G. Yao, E. Hitz, Y. J. Li, J. Q. Dai, S. M. Xu, W. Luo, E. D. Wachsman, L. B. Hu, Nano Lett. 17 (2017) 565-571.

[48] Z. Y. Guo, J. L. Li, Y. Xia, C. Chen, F. M. Wang, A. G. Tamirat, Y. G. Wang, Y. Y. Xia, L. Wang, S. H. Feng, J. Mater. Chem. A 6 (2018) 6022-6032.

[49] S. F. Liu, X. H. Xia, Y. Zhong, S. J. Deng, Z. J. Yao, L. Y. Zhang, X. B. Cheng, X. L. Wang, Q. Zhang, J. P. Tu, Adv. Energy Mater. 8 (2017) 1702322.

[50] G. Y. Jiang, N. Jiang, N. Zheng, X. Chen, J. Y. Mao, G. Y. Ding, Y. H. Li, F. G. Sun, Y. S. Li, Energy Storage Mater. (2019) *DOI: 10.1016/j.ensm.2019.05.014*.

[51] K. Li, Z. Y. Hu, J. Z. Ma, S. Chen, D. X. Mu, J. T. Zhang, Adv. Mater. 31 (2019) 1902399.

[52] G. Bieker, M. Winter, P. Bieker, Phys. Chem. Chem. Phys. 17 (2015) 8670-8679.

[53] Y. Akita, M. Segawa, H. Munakata, K. Kanamura, J. Power Sources 239 (2013) 175-180.

[54] C. Marino, A. Boulaoued, J. Fullenwarth, D. Maurin, N. Louvain, J. L. Bantignies, L. Stievano, L. Monconduit, J. Phys. Chem. C 121 (2017) 26598-26606.

[55] X. F. Lei, X. Z. Liu, W. Q. Ma, Z. Cao, Y. G. Wang, Y. Ding, Angew. Chem. Int. Ed. 57 (2018) 16131-16135.

Figures and captions

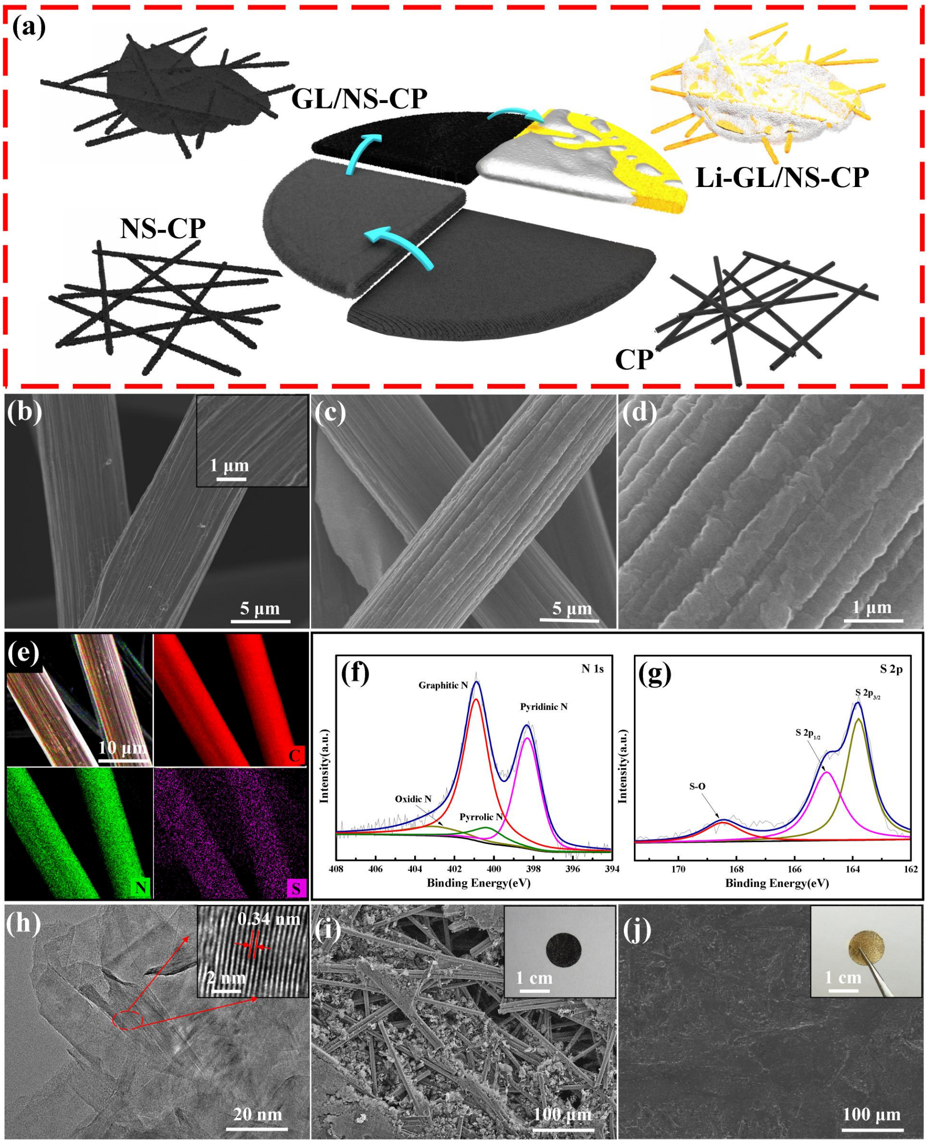

Fig. 1. (a) Schematic illustration of the preparation of Li-GL/NS-CP; SEM images of (b) pristine CP (Insert: the enlarged SEM images of CP); (c, d) SEM images with different magnifications, (e) EDX mapping images and (f, g) XPS spectra of NS-CP. (h) TEM images of GL (Insert: enlarged TEM image of GL); SEM and photo (insert) images of (i) GL/NS-CP and (j) Li-GL/NS-CP, respectively.

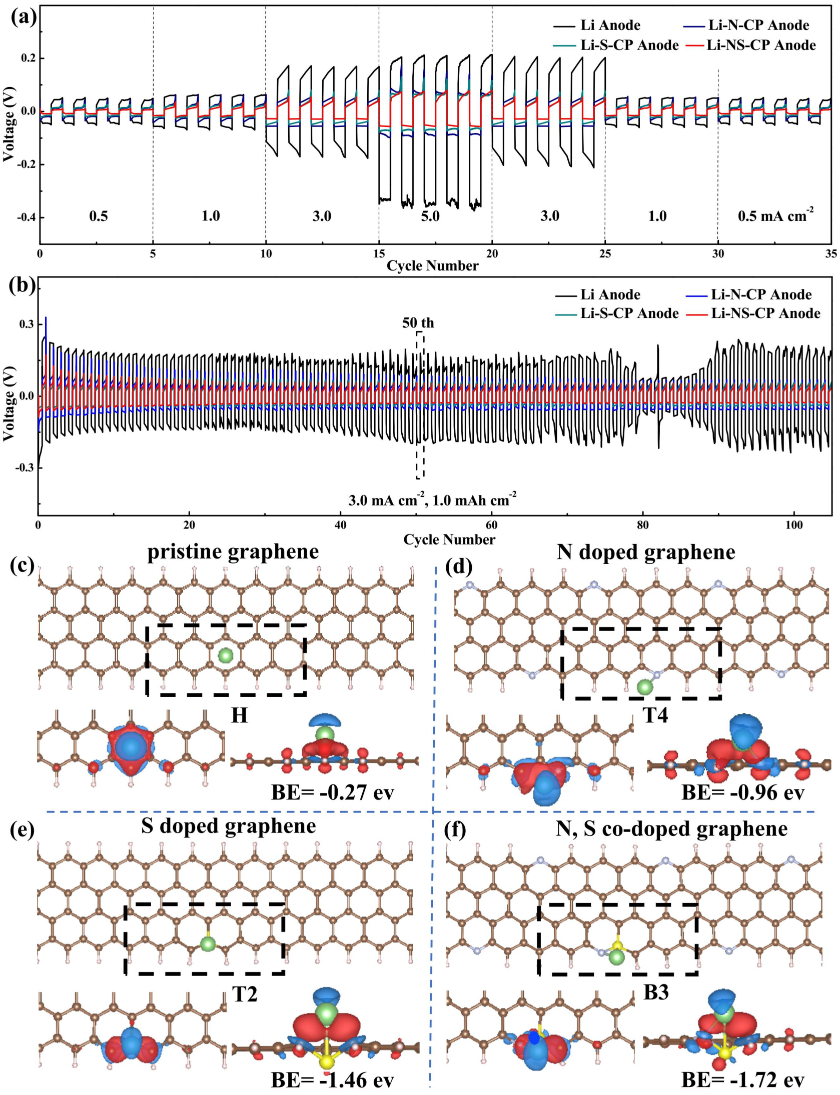

Fig. 2. (a) Voltage profiles of Li-NS-CP, Li-N-CP, Li-S-CP and bare Li anodes based symmetrical batteries at different current densities; (b) Cycling performances of Li-NS-CP, Li-N-CP, Li-S-CP and bare Li electrodes under the current density of 3.0 mA cm^{-2} with the limited capacity of 1.0 mAh cm^{-2}. Charge density differences for adsorption of Li on (c) pristine, (d) N-doped, (e) S-doped and (f) N, S co-doped graphene, respectively. C, N, S, H, and Li atoms are colored as brown, light grey, yellow, light pink and green, respectively. Regions of electron accumulation and depletion are shown in red and blue.

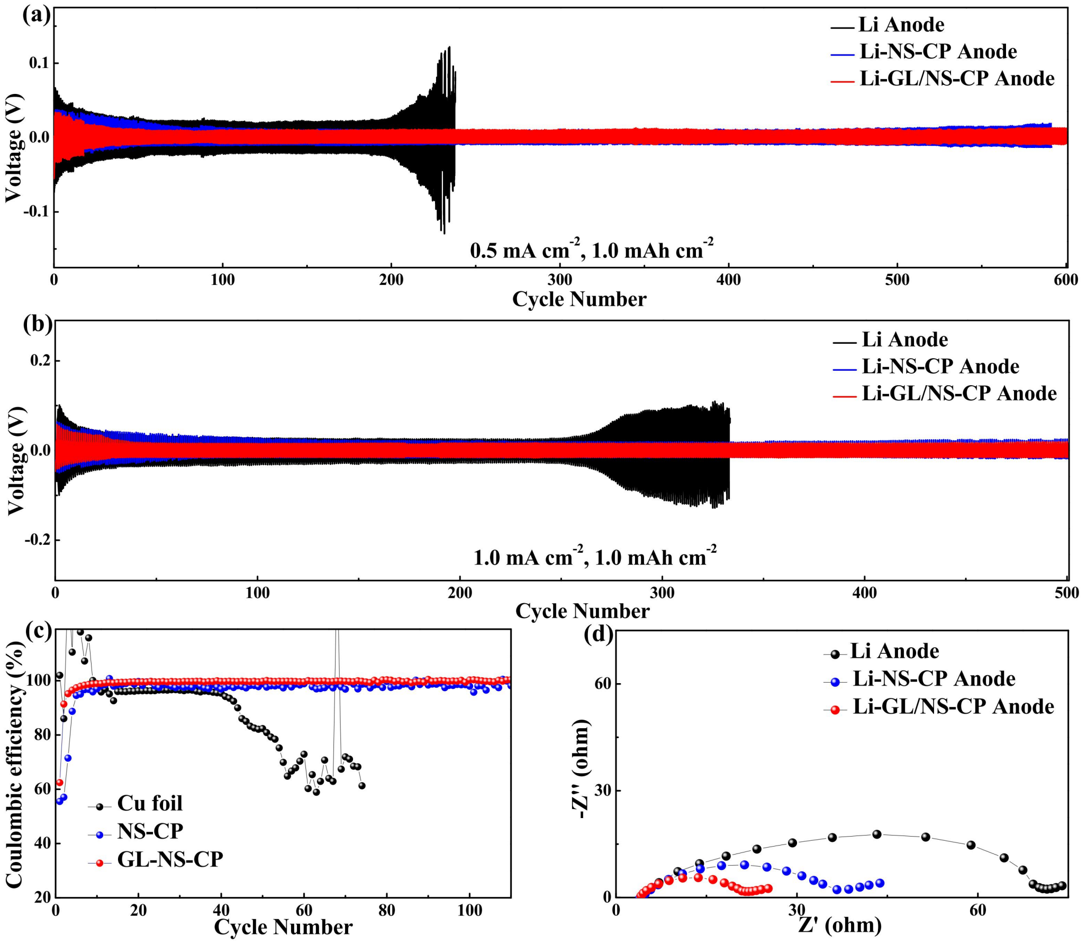

Fig. 3. Cycle stability of Li-GL/NS-CP, Li-NS-CP and bare Li electrodes in symmetrical cells under the limited stripping/plating capacity of 1.0 mAh cm^{-2} at different current densities: (a) 0.5 mA cm^{-2} and (b) 1.0 mA cm^{-2}, respectively. (c) Comparison of the Coulombic efficiencies of GL/NS-CP, NS-CP and Cu foil electrodes at 1.0 mA cm^{-2}. (d) Nyquist plots of the symmetrical cells with Li-GL/NS-CP, Li-NS-CP and bare Li anodes at 1.0 mA cm^{-2} after 10 cycles.

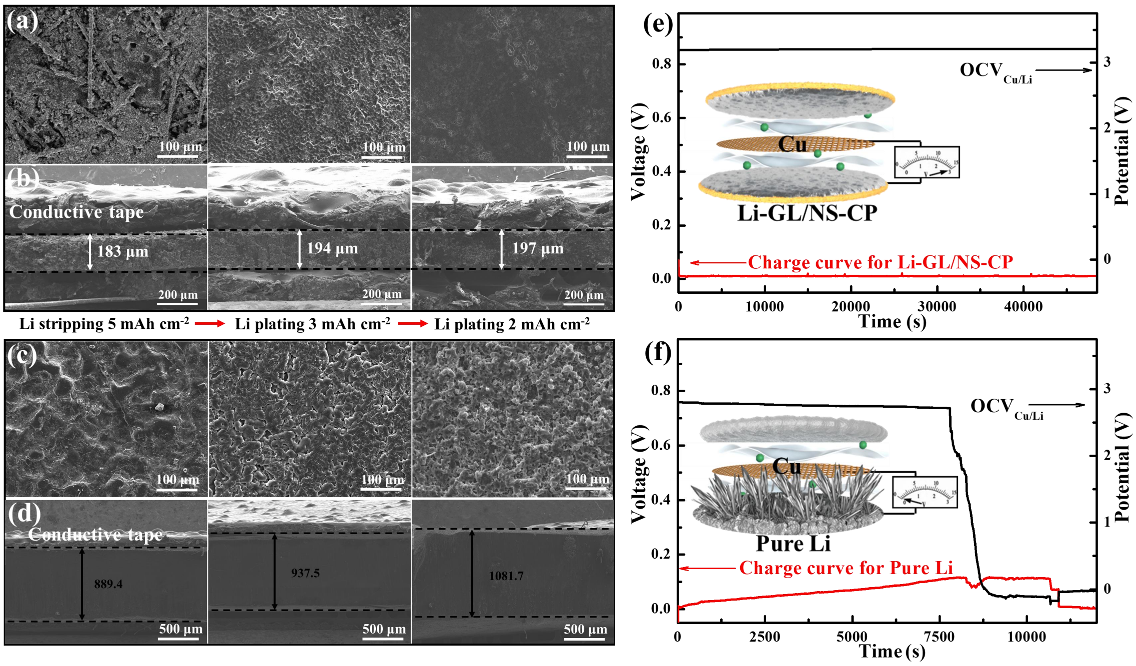

Fig. 4. (a) Top and (b) cross-sectional SEM images of Li-GL/NS-CP electrode after stripping away 5.0 mAh cm^{-2}, and then plating 3.0 mAh cm^{-2} and 2.0 mAh cm^{-2} Li back; (c) surface and (d) Cross-section SEM images of pure Li anode after the different amounts of Li stripping/plating. All the applied current densities are 1.0 mA cm^{-2}. Electrochemical performances of (e) Li-GL/NS-CP-based and (f) pure Li-based symmetric cells at the current density of 5.0 mA cm^{-2}; Insert: illustration of the internal variation of the corresponding batteries (In this test, the Li-based electrode/separator/Cu mesh/separator/Li-based electrode was sealed in a home-made cell. The operating voltage of Li-based electrode *vs.* Li-based electrode is recorded to characterize the Li plating process. The open circuit voltage (OCV) of Li-based electrode *vs.* Cu mesh (OCV$_{Cu/Li}$) is also detected during this process).

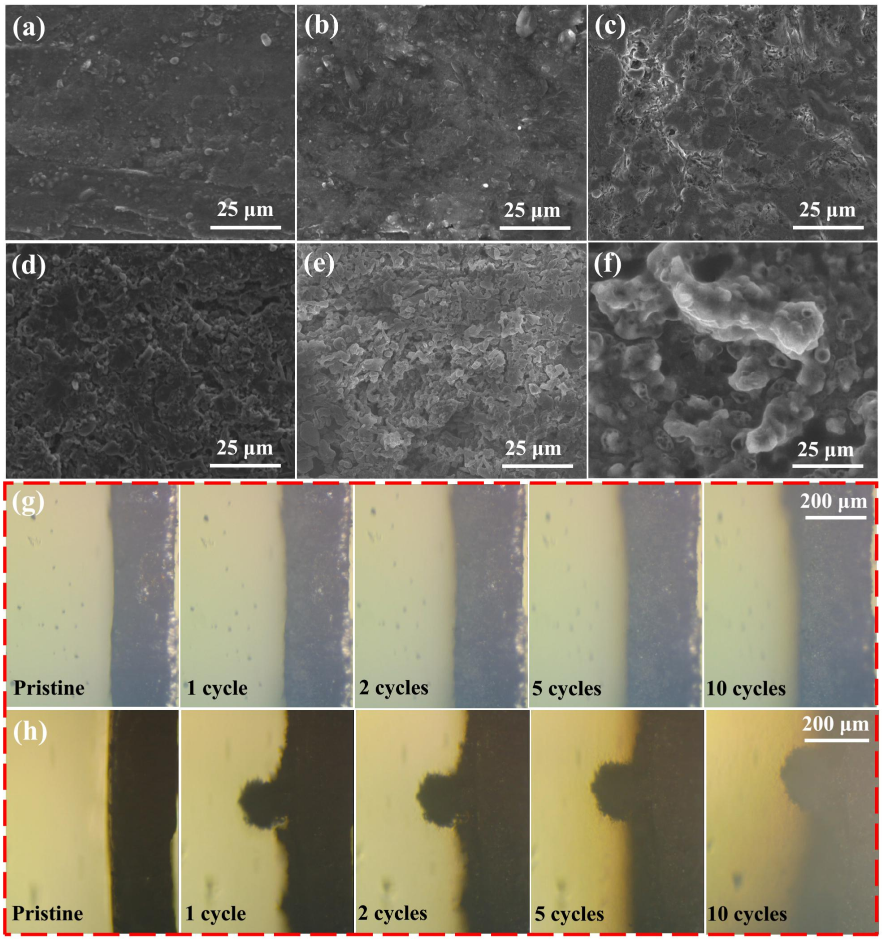

Fig. 5. SEM images of (a-c) Li-GL/NS-CP and (d-f) bare Li electrodes at a fixed capacity of 1.0 mAh cm^{-2} after 10 Li stripping/plating cycles under different current densities: (a, d) 0.5 mA cm^{-2}, (b, e) 1.0 mA cm^{-2} and (c, f) 3.0 mA cm^{-2}. The cross-sectional morphological evolutions of (g) Li-GL/NS-CP and (h) bare Li electrodes (~200 µm) at the current density of 3.0 mA cm^{-2} with the limited capacity of 1.0 mAh cm^{-2} over 10 cycles (observed by the *in situ* optical microscopy).

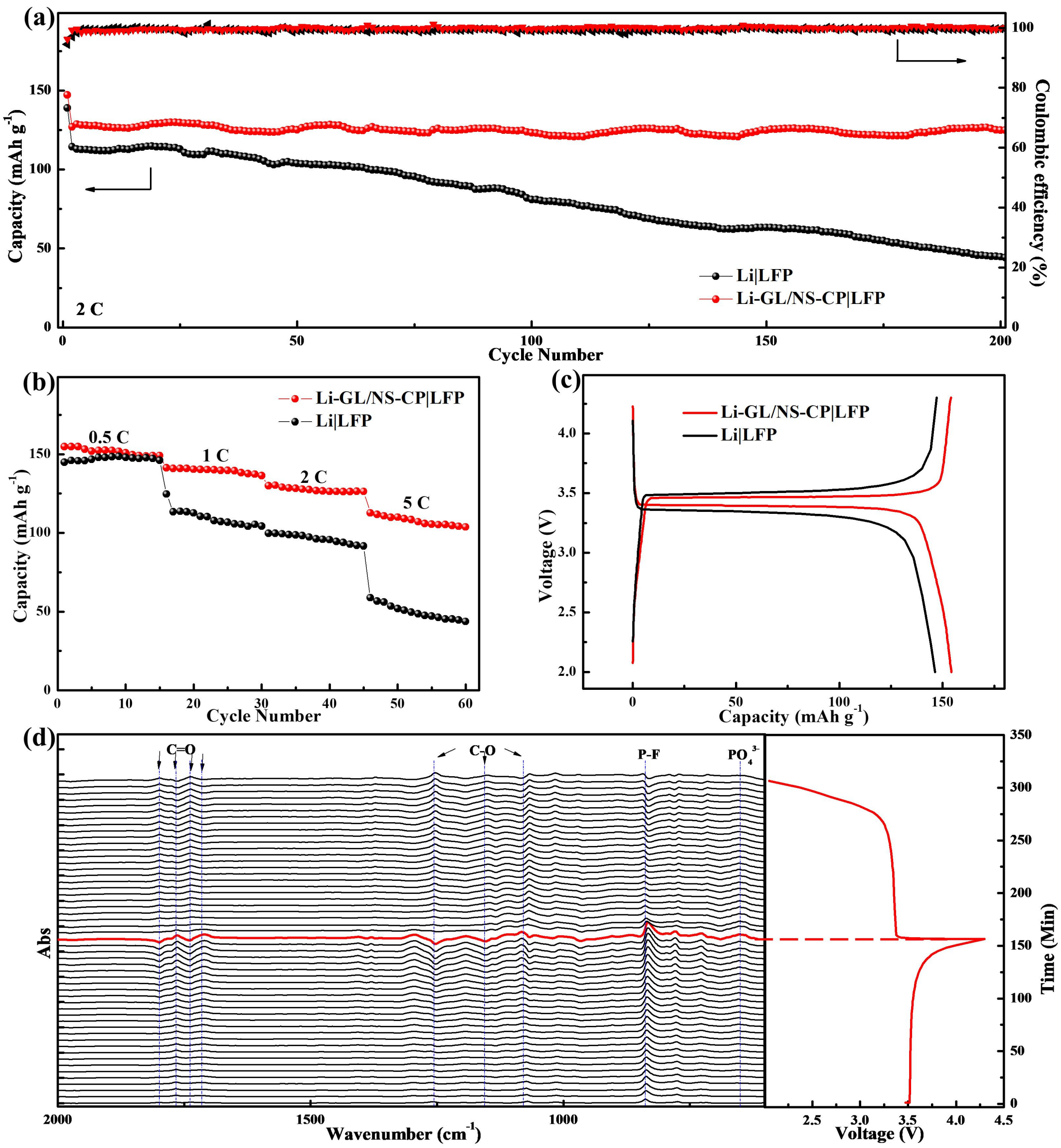

Fig. 6. (a) Discharge capacity retention and Coulombic efficiency at 2.0 C and (b) rate performance and (c) voltage curves of Li-GL/NS-CP|LFP and Li|LFP batteries at 0.5 C (1.0 C = 170 mA g^{-1} for LFP cathode). (d) *In situ* FT-IR spectra curves and the corresponding voltage curves of Li-GL/NS-CP|LFP battery at 0.3 C between 2.0 and 4.3 V.

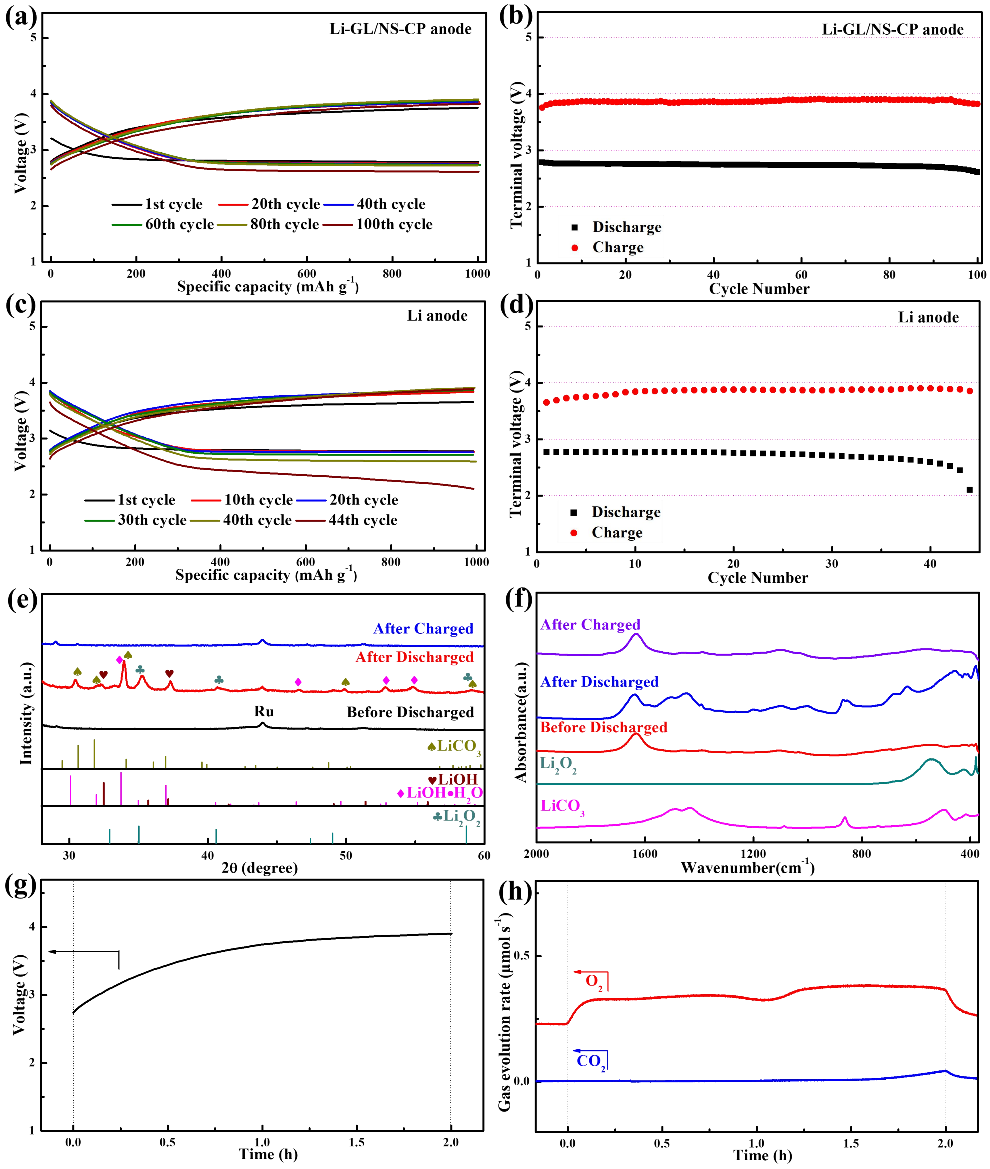

Fig. 7. (a) Discharge/charge profiles of the Li–air battery with Li-GL/NS-CP anode over different cycles and (b) the corresponding discharge and charge terminal voltages *versus* cycle number; (c) Voltage curves of the Li–air cell using pure Li anode at various cycles and (d) the corresponding voltages at the end of discharge/charge curves *versus* cycle number; All these Li–air batteries were tested at a current density of 500 mA g^{-1} with the fixed capacity of 1000 mAh g^{-1}; (e) XRD patterns and (f) *ex situ* FT-IR spectra of the cathodes before discharge, after discharge

and after recharge; (g) The charge profile of the Li-GL/NS-CP anode based Li–air battery at a current of 0.5 mA and (h) the corresponding gas evolution which is analyzed by *in-situ* DEMS.

Table of Contents

The graphite-based layer (GL) modified nitrogen (N) and sulfur (S) co-doping carbon paper (GL/NS-CP) is prepared and used as host to construct Li based GL/NS-CP electrode. Experimental and theoretical results have demonstrated that the GL/NS-CP shows the superior lithiophilicity, and thus Li-GL/NS-CP anode is capable of the suppression for both volume change and Li dendrite, and shows good electrochemical performances in Li–air batteries.

TOC Figure